Supplementary Information of "Common mode signals and vertical velocities in the great Alpine area from GNSS data" by Pintori F. et al.

S1. GPS processing

We use the GAMIT/GLOBK (Herring et al., 2018) software, and for this work in particular its 10.71 version, to analyze Global Positioning System (GPS) observations from the continuous GNSS stations shown in Fig. 1. The processing scheme is mainly based on three different steps: 1) GPS phase reduction and generation of loosely-constrained sub-network solutions, 2) combination of the daily sub-networks solutions and realization of positions in specific reference frames and 3) the time-series analysis.

Step 1 is performed using the GAMIT module of the GAMIT/GLOBK software. First, the whole RINEX dataset available each day in the archive is subdivided into smaller sub-networks, each consisting of 40 stations, plus an additional network of tie-stations (including at least one site in common with all clusters) and a cluster including all the IGb14 core sites available in the study region. Processing is conducted independently for each day and for each subnetwork. The GAMIT software uses an ionosphere-free linear combination of GPS phase observables by applying a double differencing technique to eliminate phase biases related to drifts in the satellite and receiver clock oscillators. GPS phase data are weighted according to an elevation-angle-dependent error model (Herring et al., 2018) using an iterative analysis procedure whereby the elevation dependence was determined by the observed scatter of phase residuals. In this analysis the parameters of satellite orbit are fixed to the IGS final values. IGS absolute antenna phase center models (igs14_wwww.atx, available at ftp://chandler.mit.edu/updates/source/incremental_updates/tables) for both satellite and ground-based antennas is adopted in order to improve the accuracy of vertical site position component estimations. The first-order ionospheric delay is eliminated by using the ionosphere-free linear combination, while second-order ionospheric corrections (Petrie et al., 2010) is applied using the IONEX files from the Center for Orbit Determination in Europe (CODE). The tropospheric delay is modeled as a piecewise linear model and estimated using the Vienna Mapping Function 1 (VMF1, Boehm et al., 2007) with a 10° cutoff. We use the Global Pressure and Temperature 2 (GPT2) model to provide a priori hydrostatic delays. The Earth Orientation Parameters (EOP) were tightly constrained to priori values obtained from IERS Bulletin B. The ocean tidal loading was corrected using the FES2004 model (Lyard et al., 2006).

The daily, loosely constrained, solutions of the daily sub-networks, plus the tie-network and the IGb14-core sites network, are combined using the GLOBK software, which adopts a Kalman filter estimation algorithm, simultaneously realizing a global reference frame by applying generalized constraints (Dong et al. 1998). Specifically, we define the reference frame by minimizing the velocities of the IGb14 core stations, augmented by a set of high-quality IGS stations (http://igscb.jpl.nasa.gov, accessed on 6 January 2021), while estimating a seven-parameter transformation with respect to the GPS realization of the ITRF2014 frame, i.e., the IGb14 reference frame.

In the third step the displacement time-series are analyzed in order to estimate offsets due to instrumental changes, as documented by site logs or by visual inspections, all other signals known to the largely present in GPS time series (e.g., linear trend, seasonal signals, transient signals) are left and analyzed with the vbICA.
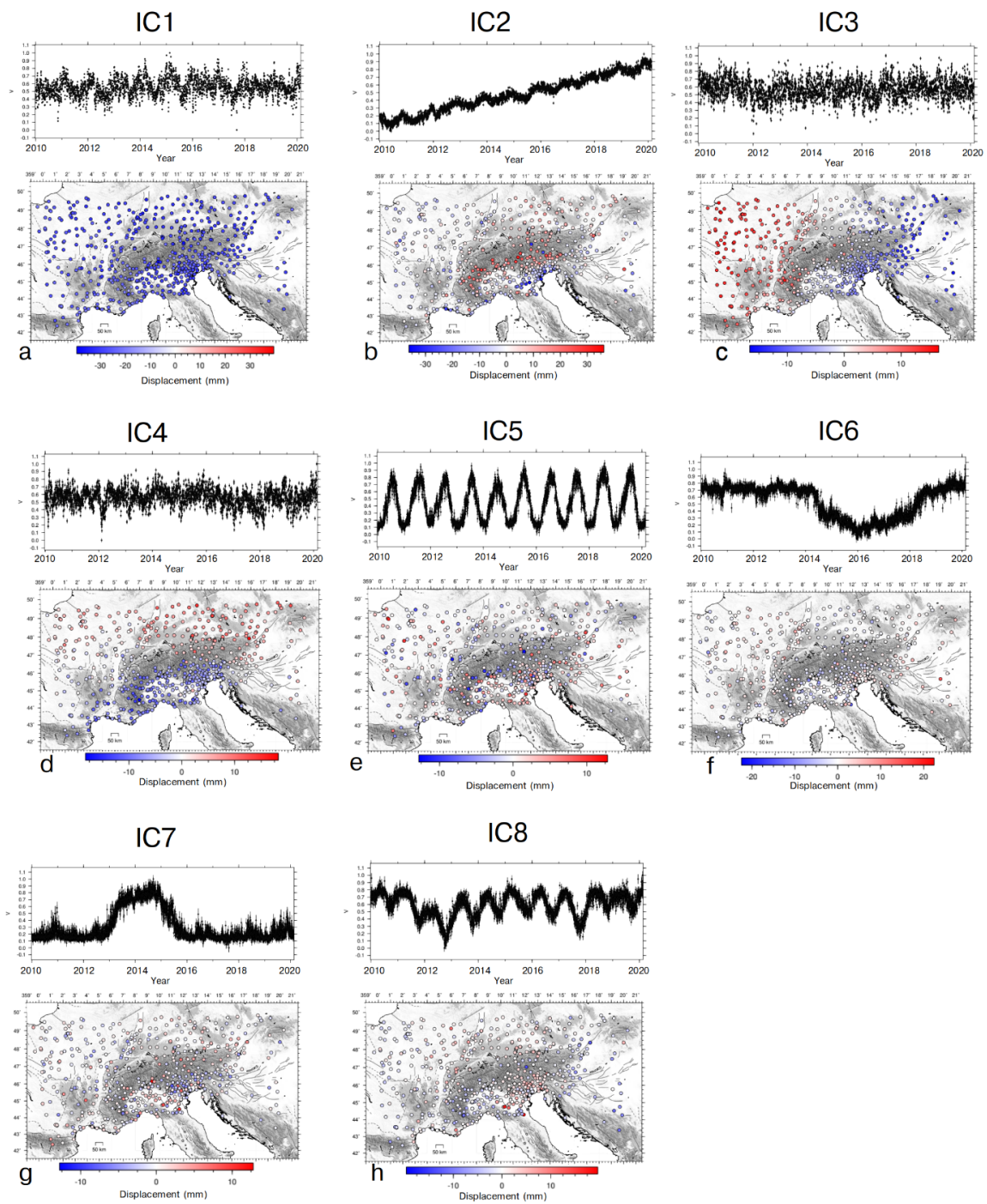
Figure S1. Temporal evolution and spatial response of: a) IC1; b) IC2; c) IC3; d) IC4; e) IC5; f) IC6; g) IC7 of the GNSS decomposition. The linear trend is not removed from the time series.
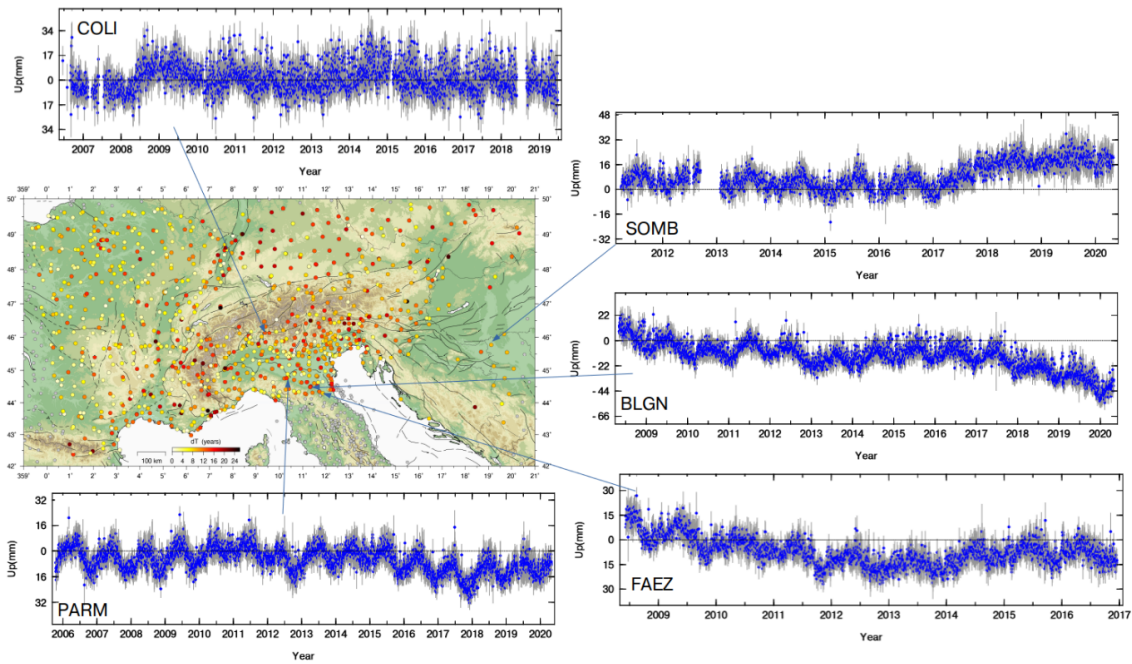
Figure S2. Temporal evolution of the vertical component of the GNSS stations most affected by IC5 (BLGN, FAEZ, SOMB); IC6 (FAEZ, PARM) and IC7 (COLI, PARM).
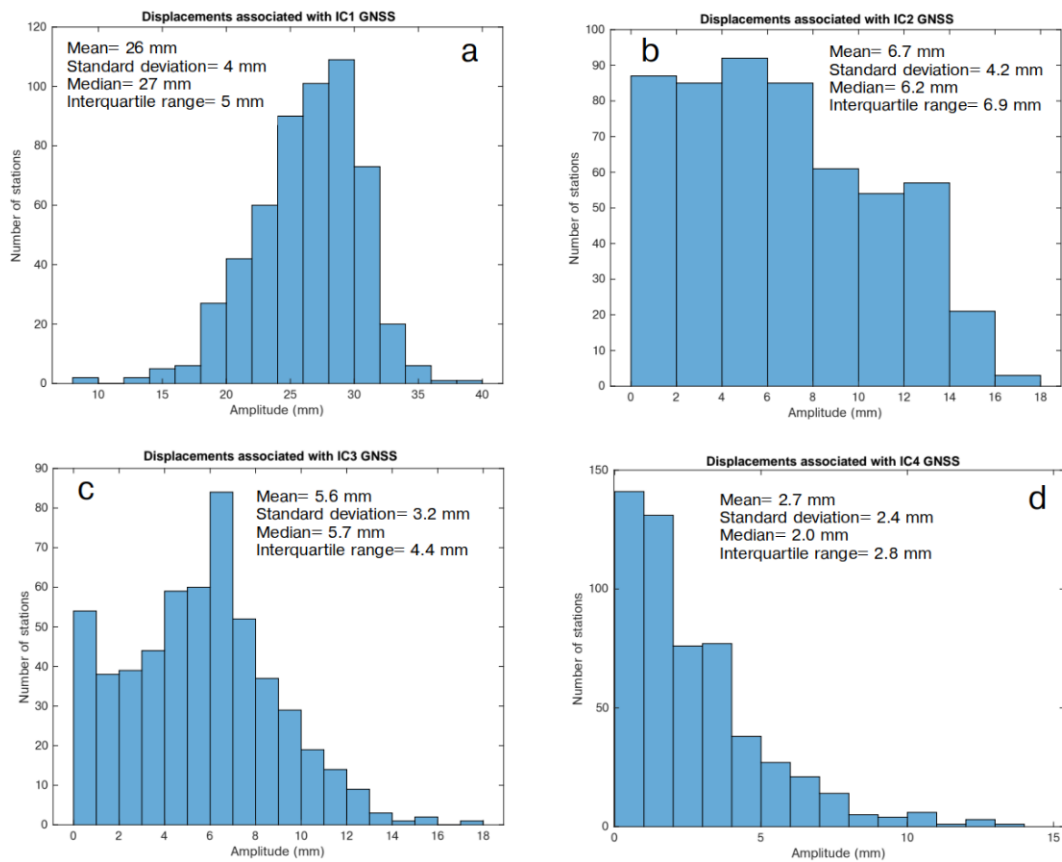

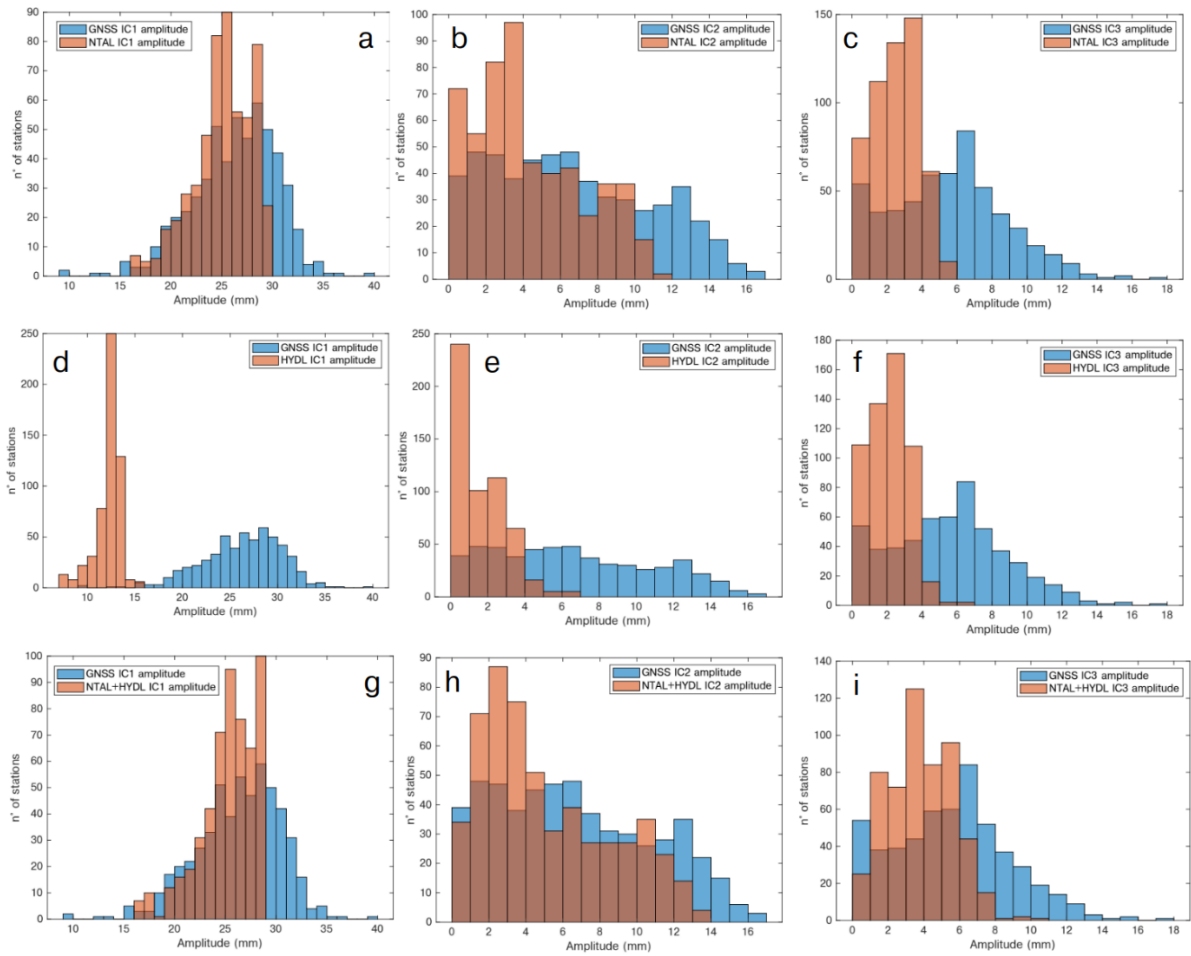**Figure S3. Histogram of the maximum displacements associated with IC1 (a); IC2 (b); IC3 (c); IC4 (d) of the GNSS decomposition.**

Figure S4. Histogram of the maximum displacements associated with IC1_NTAL (orange) compared with IC1_GNSS (blue) (a); IC2_NTAL vs IC2_GNSS (b); IC3_NTAL vs IC3_GNSS (c); IC1_HYDL vs IC1_GNSS (d); IC2_HYDL vs IC2_GNSS (e); IC3_HYDL vs IC3_GNSS (f); IC1_NTAL+HYDL vs IC1_GNSS (g); IC2_NTAL+HYDL vs IC2_GNSS (h); IC3_NTAL+HYDL vs IC3_GNSS (i).
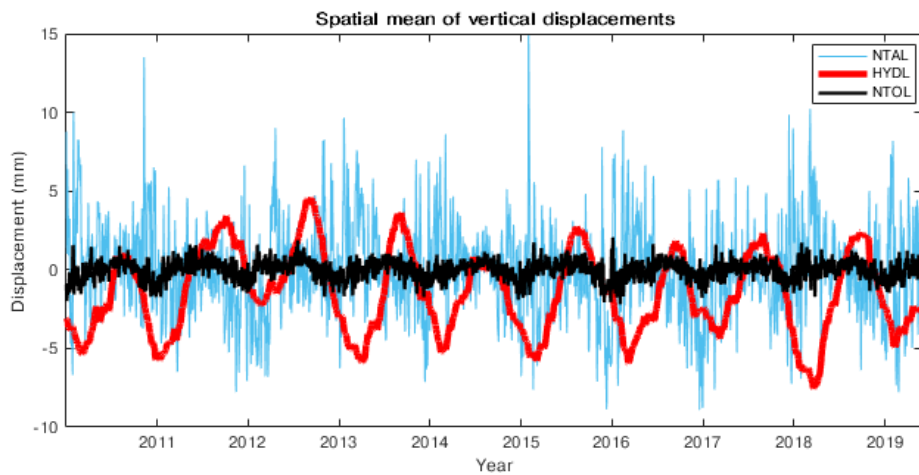

Figure S5. Spatial mean of the displacements associated with the non-tidal atmospheric (blue); hydrological (red); and non-tidal ocean (black) loading, computed using the datasets provided by LSDM (http://rz-vm115.gfz-potsdam.de:8080/repository), which are named NTAL, HYDL and NTOL.
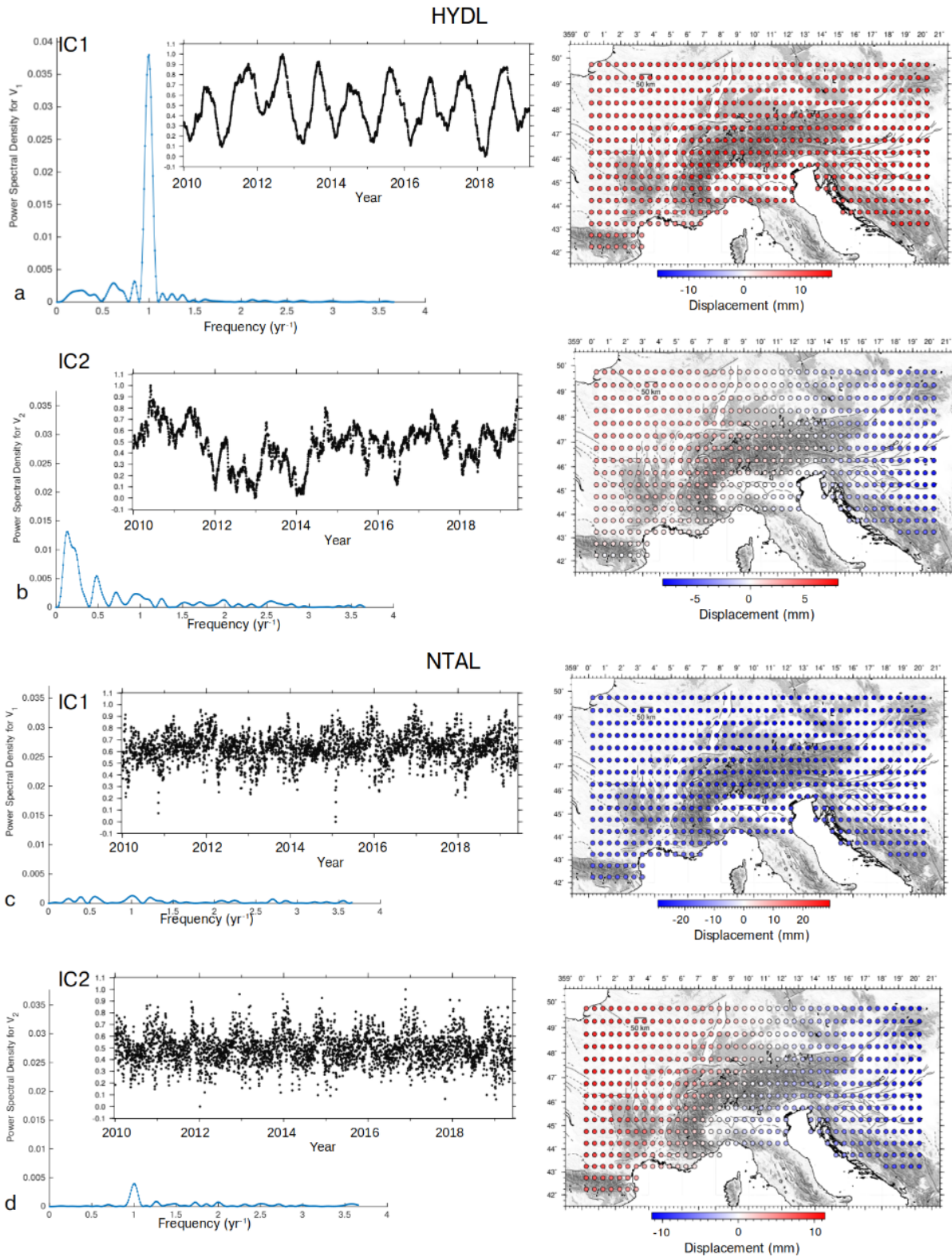
Figure S6. Temporal evolution, power spectral density and spatial response of: a) IC1; b) IC2 of the HYDL dataset, using a 2-component decomposition. c); d) are the same for the NTAL dataset, using a 2-component decomposition.
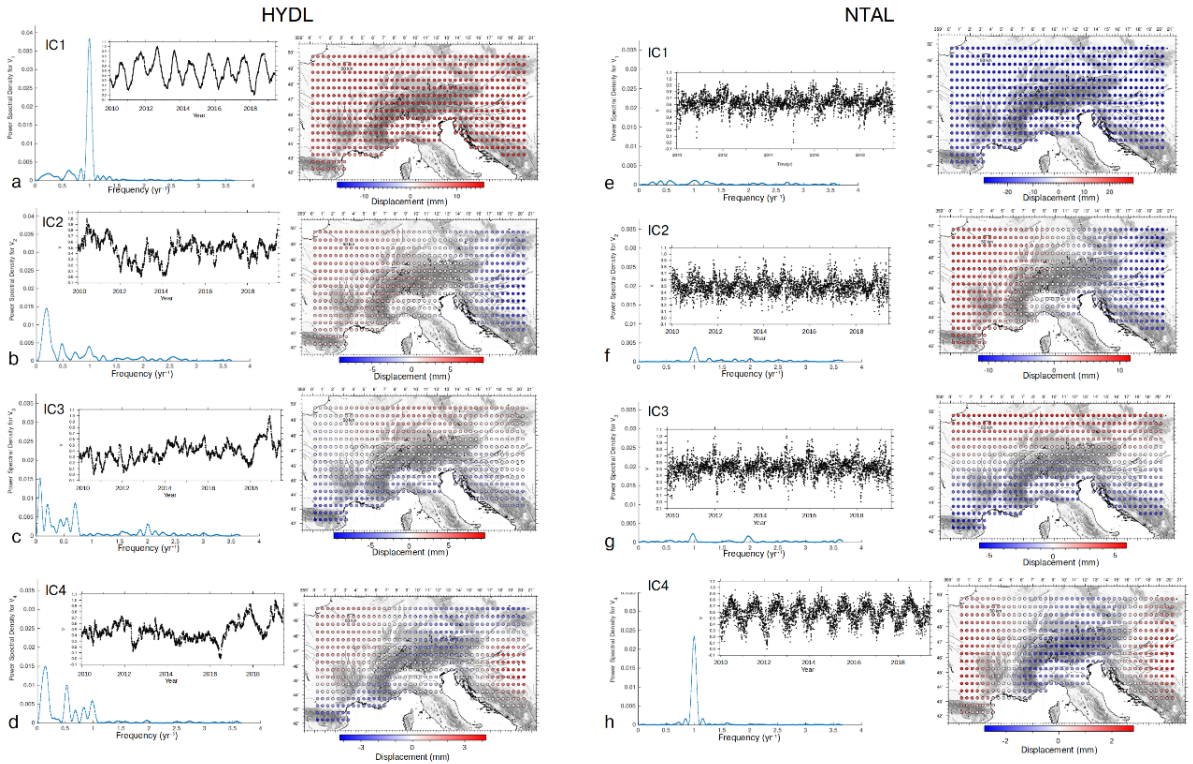
Figure S7. Temporal evolution, power spectral density and spatial response of: a) IC1; b) IC2; c) IC3; d) IC4 of the HYDL dataset, using a 4-component decomposition. e); f); g); h) are the same for the NTAL dataset, using a 4-component decomposition.
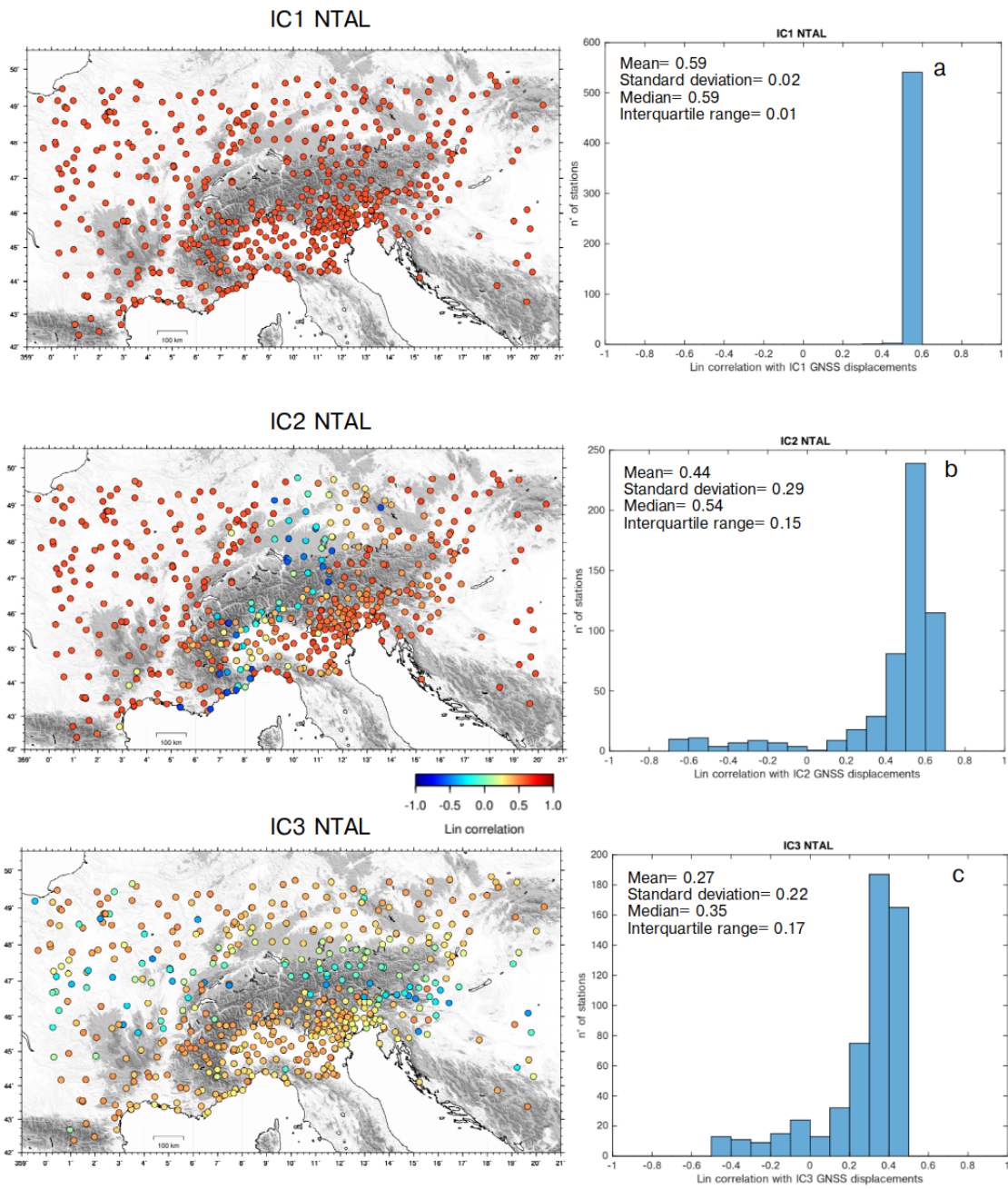
Figure S8. Lin correlation coefficients between: a) GNSS-IC1 and NTAL_IC1; b) GNSS_IC2 and NTAL_IC2; c) GNSS-IC3 and NTAL_IC3. Histograms of the correlation coefficients are also reported.
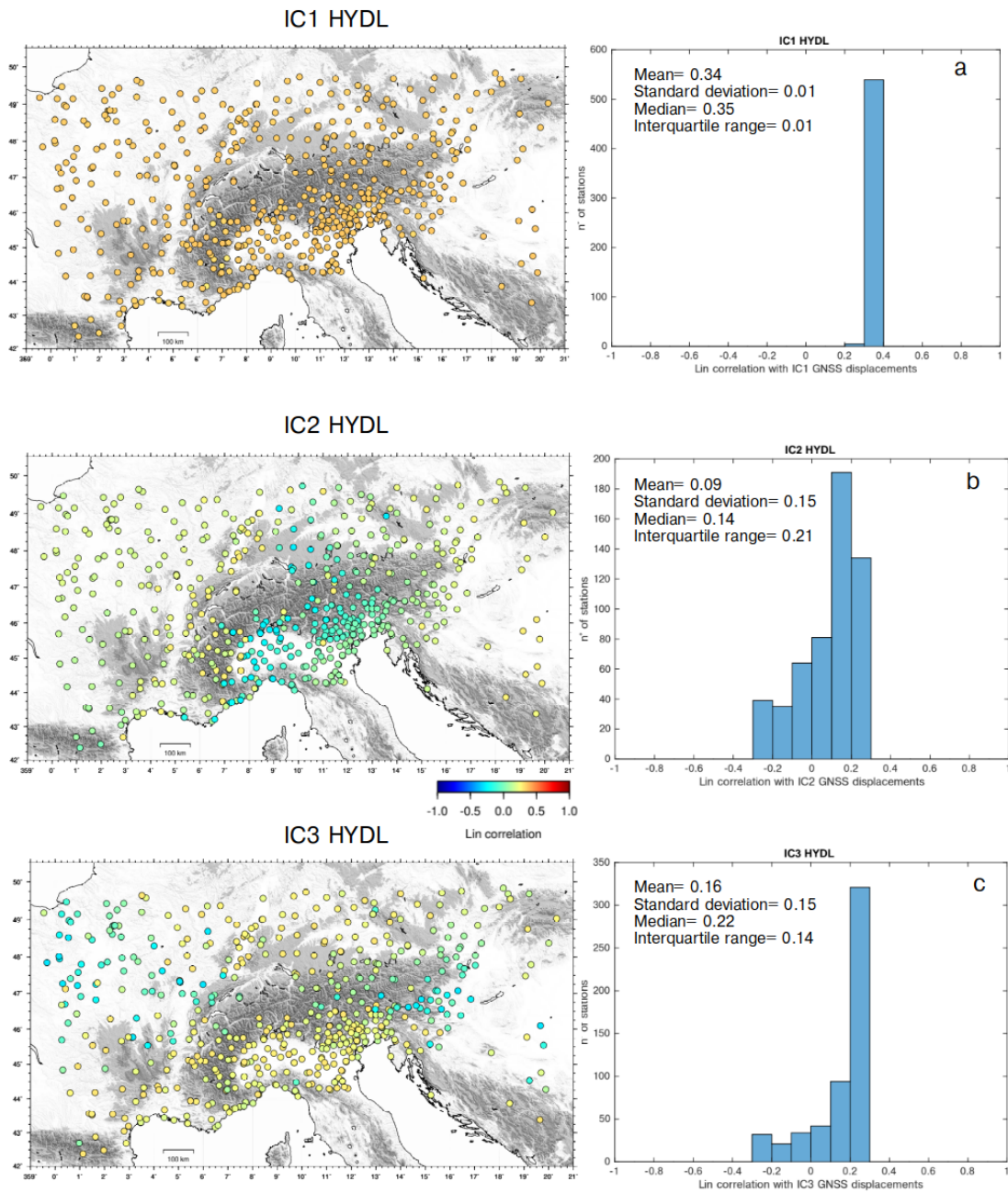
Figure S9. Lin correlation coefficients between: a) GNSS-IC1 and HYDL_IC1; b) GNSS_IC2 and HYDL_IC2; c) GNSS-IC3 and HYDL_IC3. Histograms of the correlation coefficients are also reported. The uncertainty associated with the mean values is 1σ, while the uncertainty associated with the median values is the interquartile range.

S2. Analysis of the EOST dataset and its relation with the GNSS data

In section 4.2 we interpret the GNSS displacements associated with IC1, IC2 and IC3 as induced by the combined effect of the atmospheric and hydrological loading. In that section we used the LSDM dataset as reference, here we use the EOST one.

We repeat the same workflow, performing a vbICA on the displacements associated with the atmospheric loading (ATMIB) and the hydrological loading (HYDRO). Both the temporal evolution and the spatial distribution of the ICs (Fig. S10 and S11) are very similar to the ones extracted from the EOST dataset (Fig. 4, 5).

As a consequence, the Lin correlation between the displacements of the combined ATMIB+HYDRO datasets and the GNSS ones (Fig. S12) is slightly higher than what we show in the main text (Fig. 6).
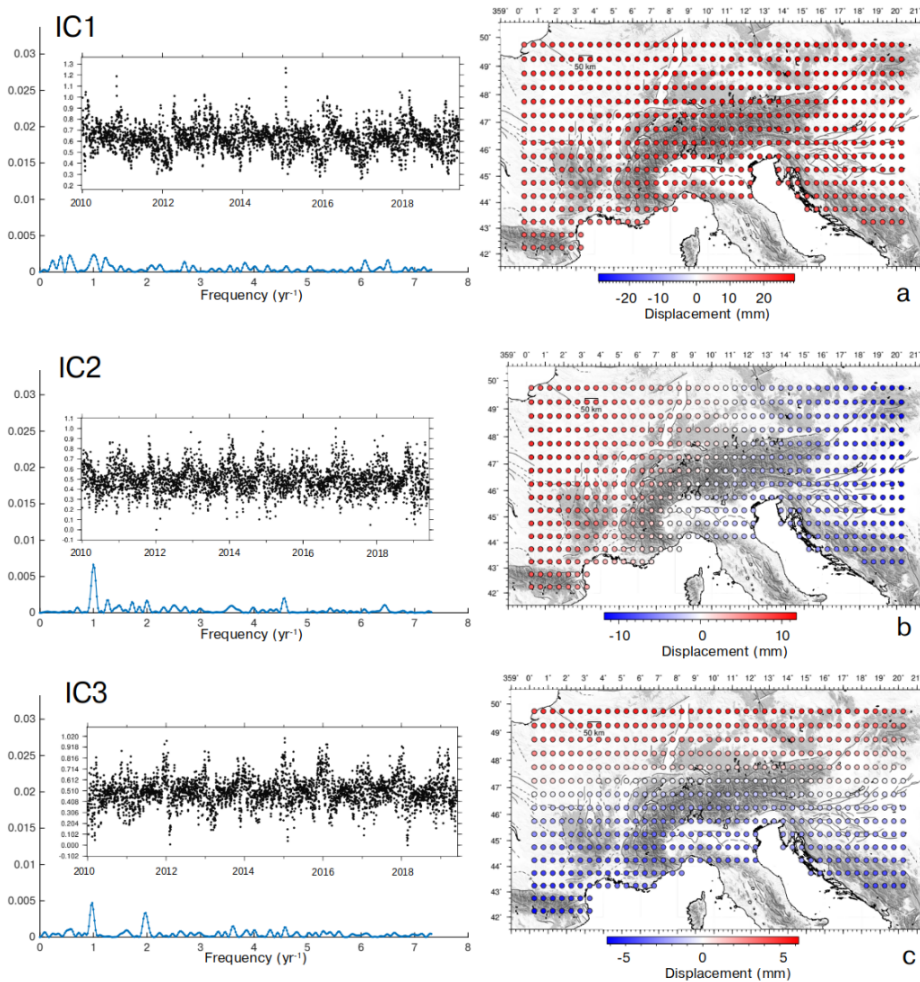

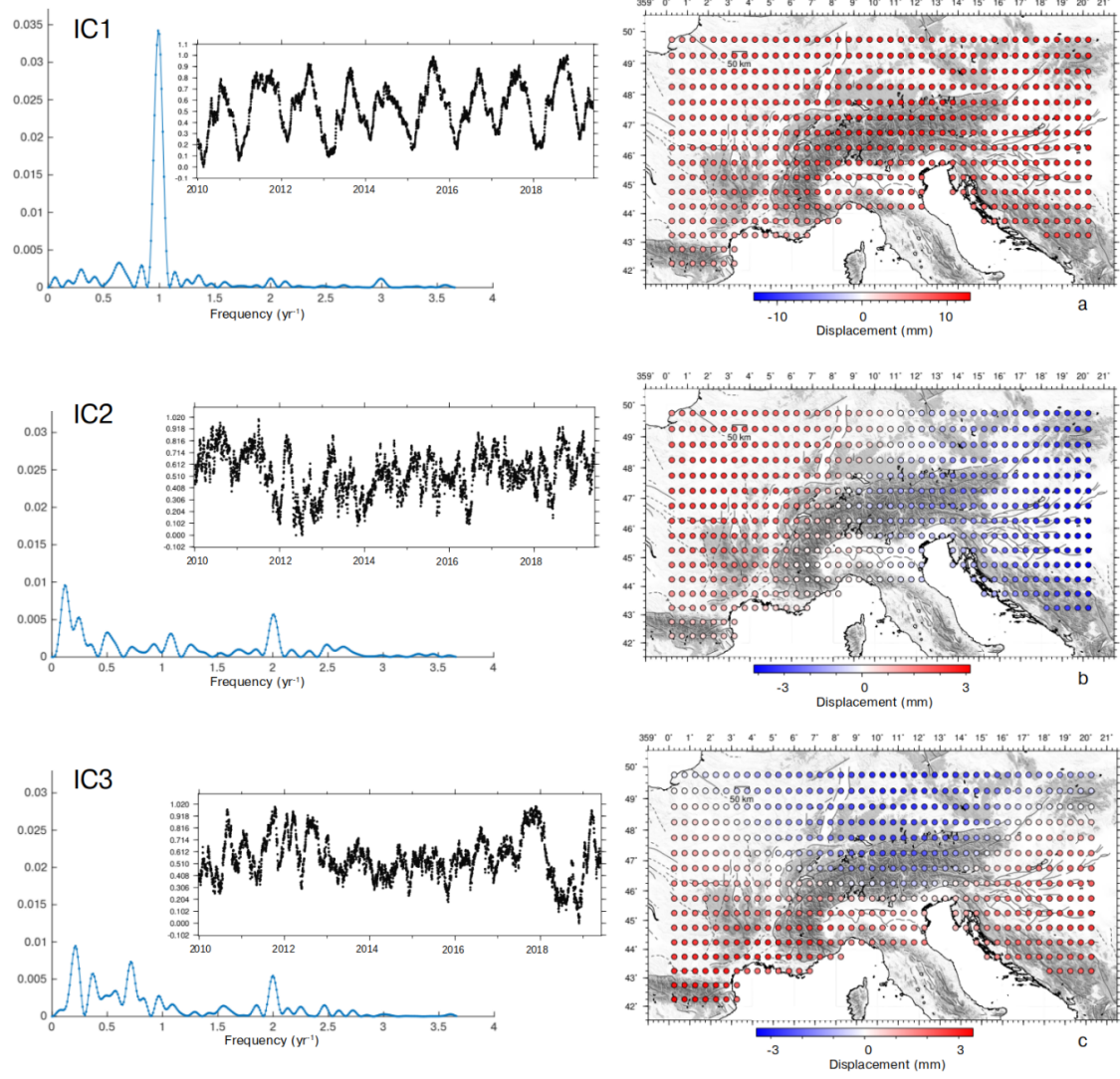**Figure S10. Temporal evolution, power spectral density and spatial response of IC1, IC2, IC3 of the ATMIB dataset.**

Figure S11. Temporal evolution, power spectral density and spatial response of IC1, IC2, IC3 of the HYDRO dataset.
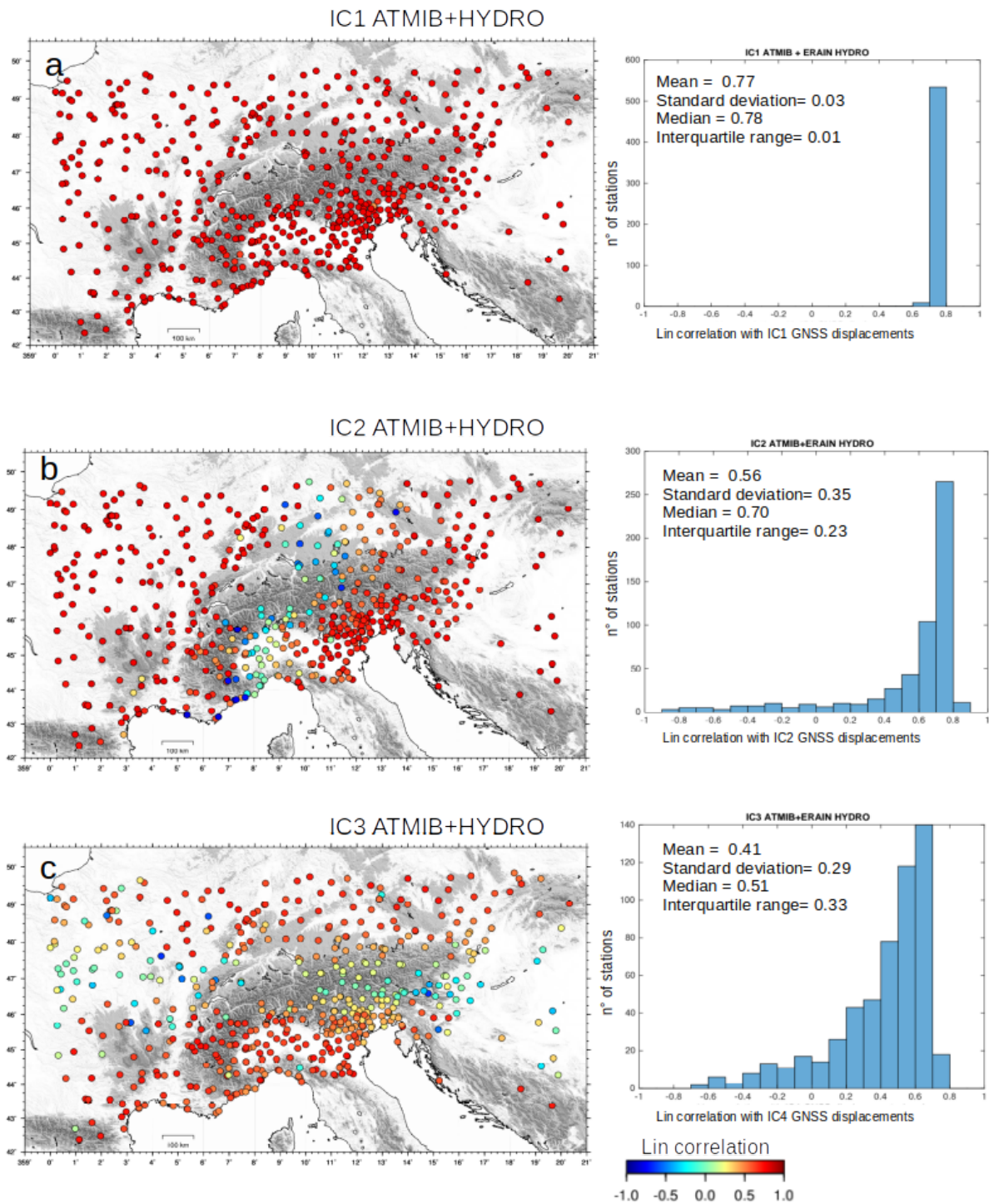
Figure S12. Lin correlation coefficients between: a) GNSS-IC1 and ATMIB+HYDRO_IC1; b) GNSS_IC2 and ATMIB+HYDRO_IC2; c) GNSS-IC3 and ATMIB+HYDRO_IC3. Histograms of the correlation coefficients are also reported.
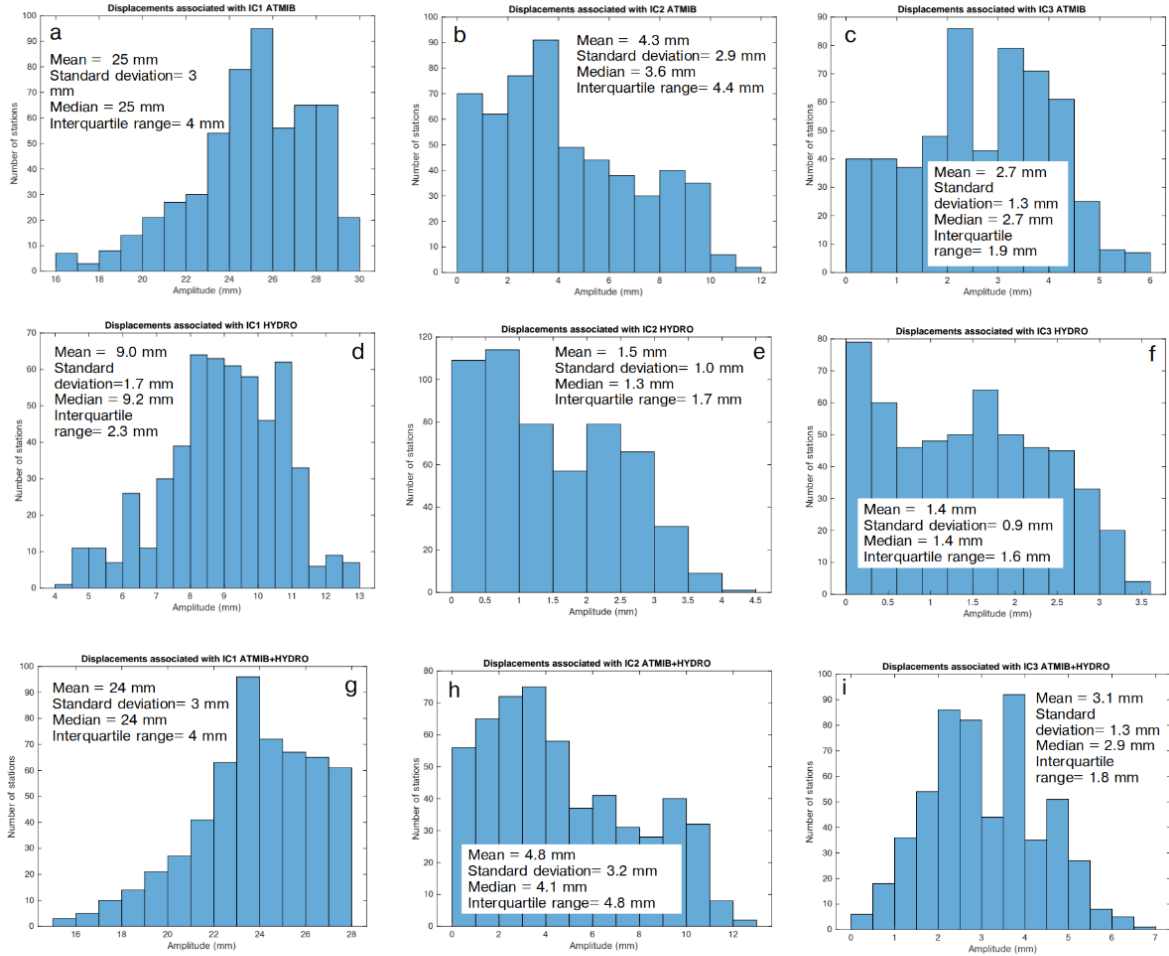
Figure S13. Histogram of the maximum displacements associated with IC1_ATMIB (a); IC2_ATMIB (b); IC3_ATMIB (c); IC1_HYDRO (d); IC2_HYDRO (e); IC3_HYDRO (f); IC1_ATMIB+HYDRO (g); IC2_ATMIB+HYDRO (h); IC3_ATMIB+HYDRO (i). The uncertainty associated with the mean values is 1σ, while the uncertainty associated with the median values is the interquartile range.

S3. Analysis of the IC5, IC6, IC7

The last three components resulting from the vbICA analysis on the detrended displacement time-series (Figure S14) appear to be associated with more localized phenomena (monument instabilities or local hydrology). IC5 and IC7, in particular, are associated with a few stations whose trend of subsidence/uplift is not constant in time (COLI, PARM, BLGN, FAEZ, SOMB, which are plotted in Fig. S2). This is due to the presence of non-linear signals, which are probably caused by some local process that we do not further investigate.

Finally, IC6 is an annual signal whose amplitude is large in particular at two GNSS sites in the Po plain (FAEZ and PARM, Fig. S2), where water withdrawal in industrial areas has been proposed by (Nespoli et al. 2021) to explain the seasonal component represented by IC6.
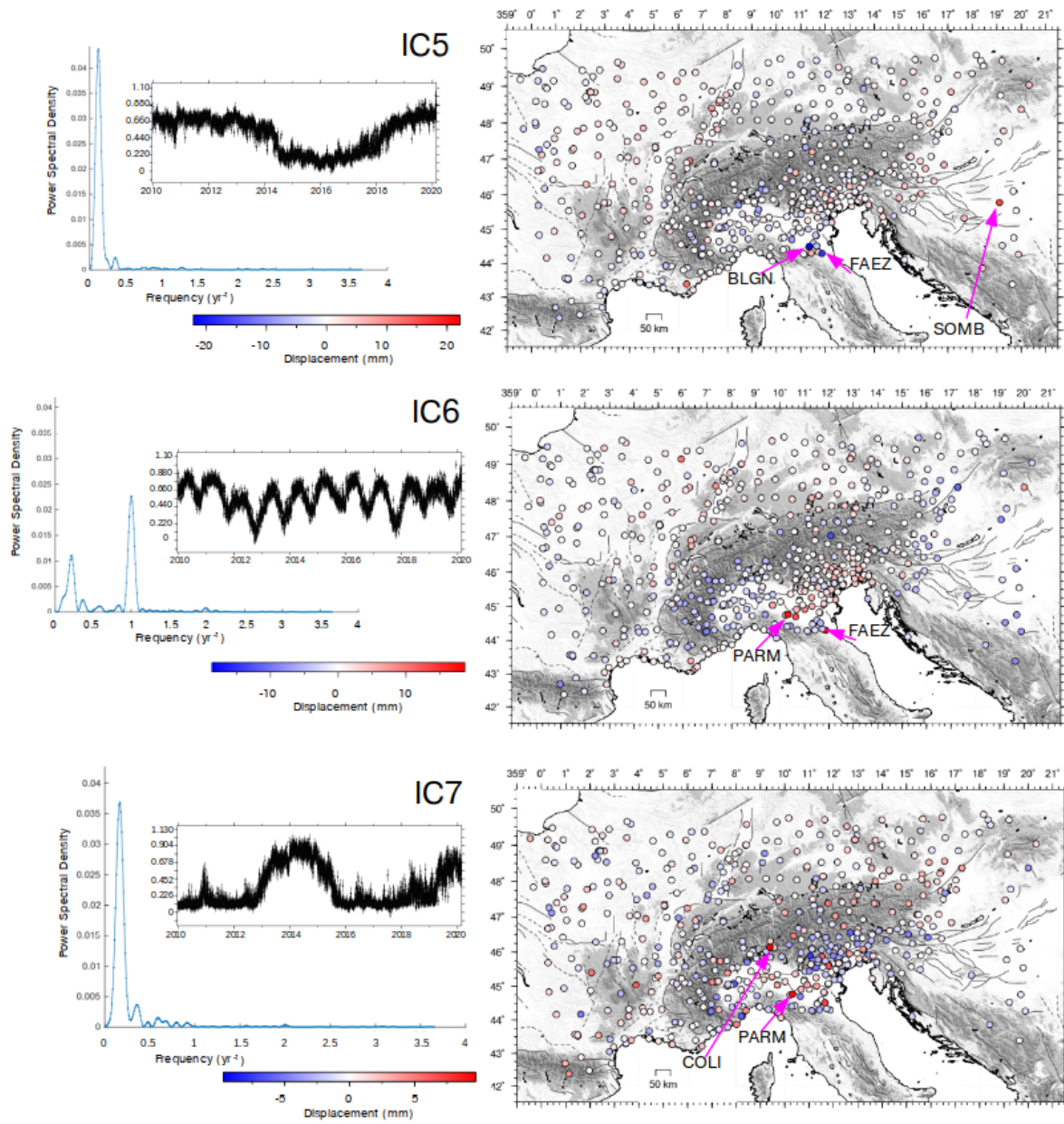
Figure S14. Temporal evolution and spatial response of IC5, IC6, IC7.
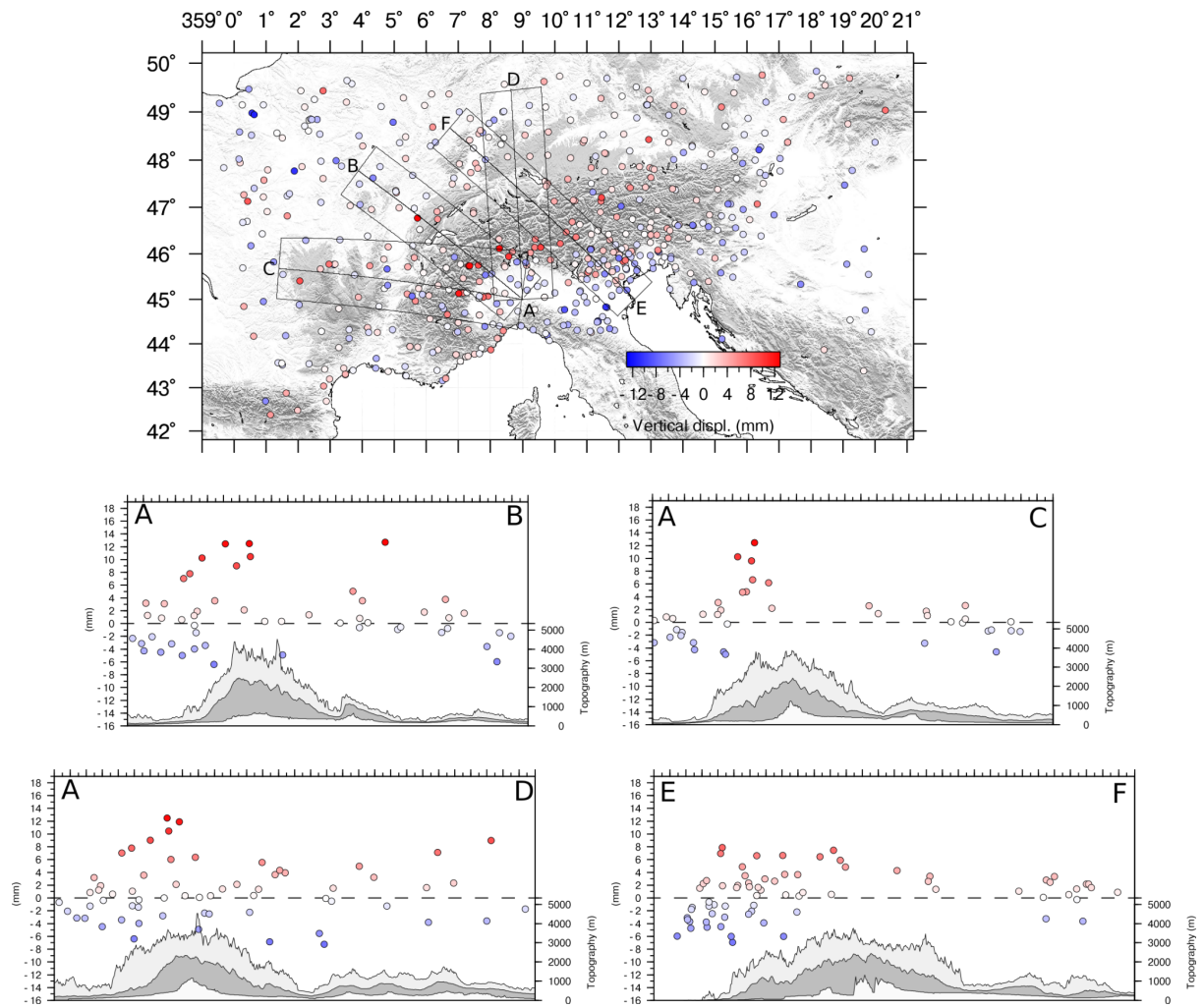
Figure S15. Cross sections showing the maximum displacements associated with IC4 across the Alps during the time interval that goes from summer 2015 to winter 2016 (see also Fig. 8).
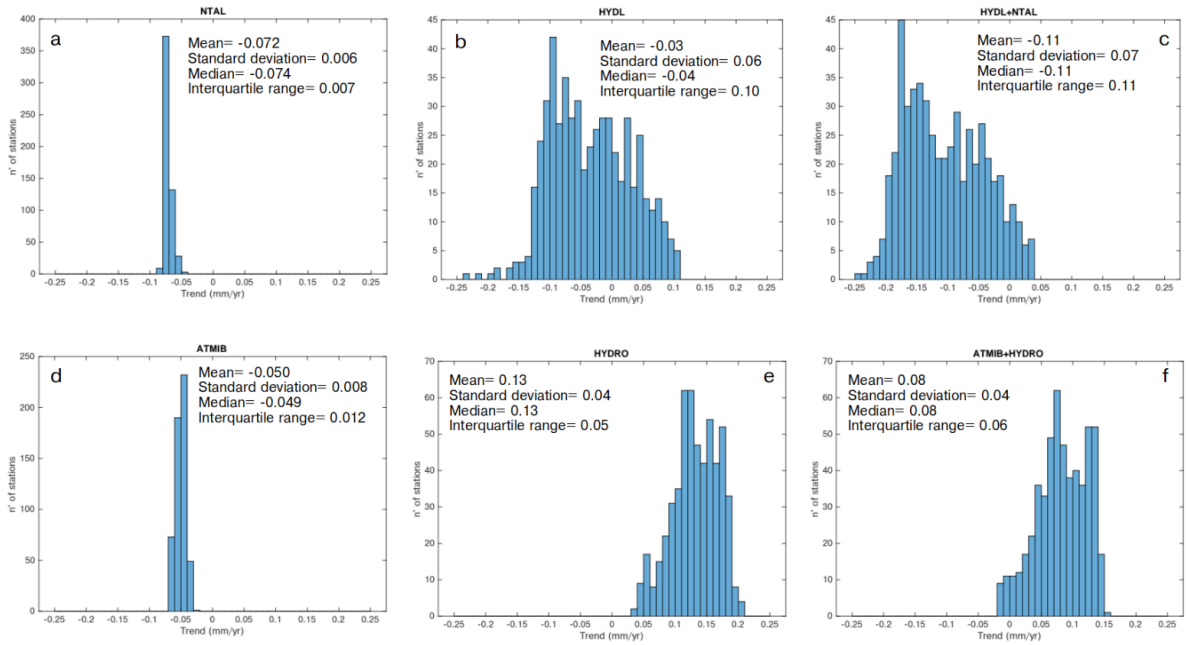
Figure S16. Histogram of the trend of: a) NTAL; b) HYDL; c) NTAL+HYDL; d) ATMIB; e) HYDRO; f) ATMIB+HYDRO.
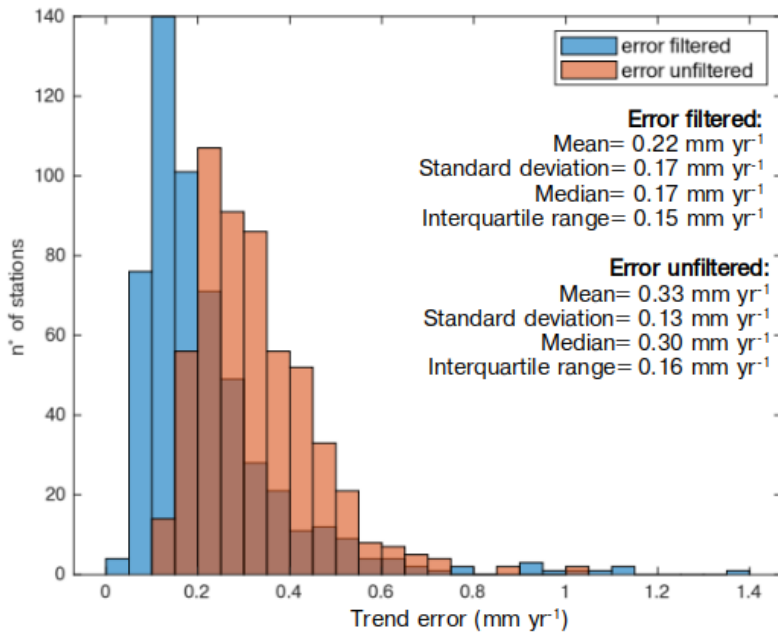

Figure S17. Histogram of the error associated with the trend of the filtered (blue) and unfiltered (orange) time series.
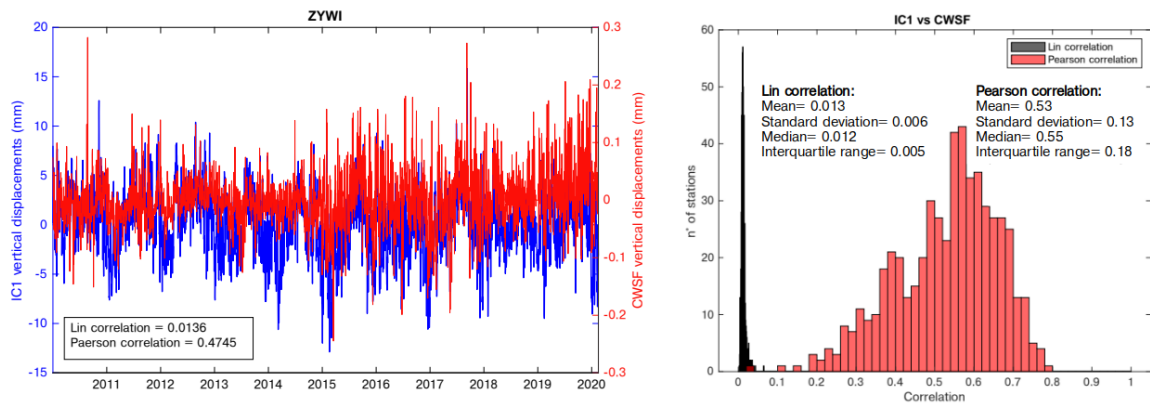
Figure S18. Comparison between the displacement associated with IC1 (in blue) at the ZYWI site and the CME estimated with the Correlation Weighted Stacking Filtering Method (in red). We also show the histogram representing the Lin (in black) and Pearson (in red) correlation between the displacements associated with the IC1 and the CME estimated with the Correlation Weighted Stacking Filtering Method at each site.
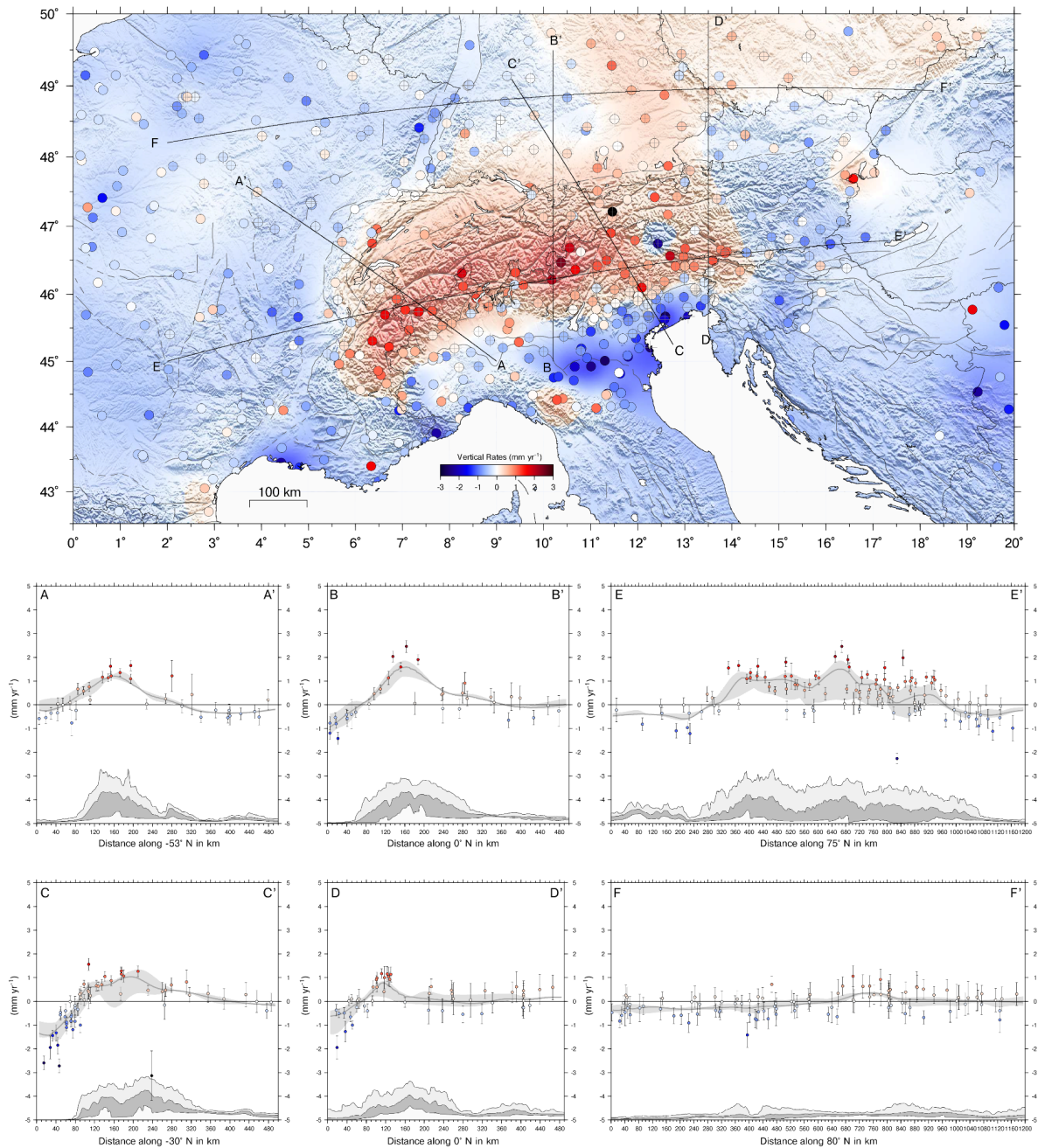
Figure S19. Vertical velocities from unfiltered time-series (colored circles), continuous velocity field, topographic and swath profiles across the great Alpine area. Each profile encompasses a 100 km swath.

References

Boehm, J., Mendes Cerveira, P. J.,   Schuh, H., and Tregoning, P.: The impact of mapping functions for the neutral atmosphere based on numerical weather models in GPS data analysis, IAG Symop. Ser., vol. 130, edited by P. Tregoning and C. Rizos, pp. 837–843, Springer, New York, 2007.

Dong, D., Herring, T. A. and King, R. W.: Estimating regional deformation from a combination of space and terrestrial geodetic data. J Geod 72:200–214. https://doi.org/10.1007/s001900050161, 1998.

Herring, T. A., King, R. W., Floyd, M. A. and McClusky, S. C.: Introduction to GAMIT/GLOBK, Release 10.7.

Retrieved from http://geoweb.mit.edu/gg/Intro_GG.pdf, 2018.

Lyard, F., Lefévre, F., Letellier, T. and Francis, O.: Modelling the global ocean tides: Modern insights from FES2004. Ocean Dynam 56(5-6):394-415, https://doi.org/10.1007/s10236-006-0086-x, 2006.

Petrie, E. J., King, M. A., Moore, P. and Lavallée, D. A.: Higher‑order ionospheric effects on the GPS reference frame and velocities. J. Geophys. Res. Solid Earth, 115(B3), http://dx.doi.org/10.1029/2009JB006677, 2010.